



Science Arts & Métiers (SAM)

is an open access repository that collects the work of Arts et Métiers Institute of Technology researchers and makes it freely available over the web where possible.

This is an author-deposited version published in: <https://sam.ensam.eu>
Handle ID: <http://hdl.handle.net/10985/24604>

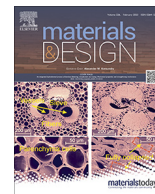
To cite this version :

Timothée DELACROIX, Fernando LOMELLO, Frederic SCHUSTER, Hicham MASKROT, Vincent JACQUIER, Pierre LAPOUGE, FREDERIC COSTE, Jean Paul GARANDET - Measurement of powder bed oxygen content by image analysis in laser powder bed fusion - Materials & Design - 2023

Any correspondence concerning this service should be sent to the repository

Administrator : scienceouverte@ensam.eu





Measurement of powder bed oxygen content by image analysis in laser powder bed fusion

Timothée Delacroix^{a,*}, Fernando Lomello^a, Frédéric Schuster^b, Hicham Maskrot^a, Vincent Jacquier^a, Pierre Lapouge^c, Frédéric Coste^c, Jean-Paul Garandet^d

^a Université Paris-Saclay, CEA, Service d'Études Analytiques et de Réactivité des Surfaces, 91191 Gif-sur-Yvette, France

^b Université Paris-Saclay, CEA, Cross-Cutting Program on Materials and Processes Skills, 91191 Gif-sur-Yvette, France

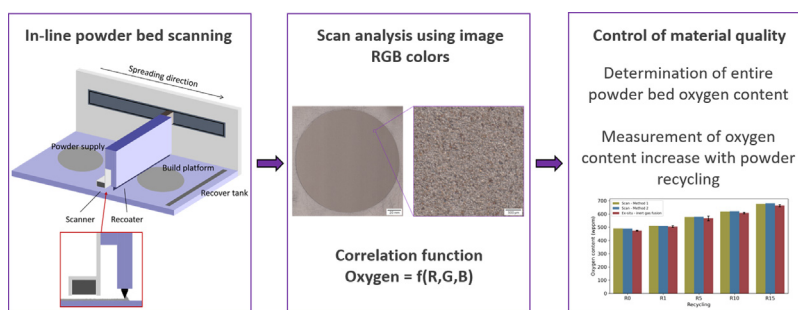
^c PIMM, Arts Et Métiers Institute of Technology, CNRS, CNAM, HESAM University, 75013 Paris, France

^d Université Grenoble Alpes, CEA, LITEN, DTNM, F-38000 Grenoble, France

HIGHLIGHTS

- Development of an in situ monitoring technique for powder bed oxygen content.
- Calibration based on correlation between particles colors and powder oxygen concentration.
- In-line measurement of recycled powders oxygen content successfully in accordance with ex-situ characterization.

GRAPHICAL ABSTRACT



ARTICLE INFO

Article history:

Received 6 October 2022

Revised 11 January 2023

Accepted 26 January 2023

Available online 28 January 2023

Keywords:

Laser powder bed fusion

Powder oxidation

Monitoring

Powder bed scanning

Image analysis

ABSTRACT

Costs and resource efficiency of laser powder bed fusion (L-PBF) are highly dependent on the ability to produce high quality parts with recycled powders. There is a need to control the quality of the material, which has a direct influence on the performance of the printed parts. Particles oxidation is known to increase with repeated powder recycling and can be a good indicator of powder degradation. The characterization of powders oxygen content is time-consuming, expensive, and usually carried out ex-situ on non-reusable quantities that are not necessarily representative of the entire feedstock. In this work, a new methodology was developed to measure the oxygen content of powders by in-line scanning of powder bed layers. The method takes advantage of stainless steel particles coloration related to their oxidation level in order to assess their oxygen concentration as a function of Red, Green and Blue channel values of image scans. The calibration procedure once carried out, several recycled powder samples were scanned and analyzed, and the determined powder beds oxygen contents were demonstrated to be in accordance with ex-situ measurements. The results highlight a new opportunity to monitor and evaluate powder degradation in-situ on powder bed layers by image analysis.

© 2023 The Authors. Published by Elsevier Ltd. This is an open access article under the CC BY-NC-ND license (<http://creativecommons.org/licenses/by-nc-nd/4.0/>).

1. Introduction

Laser Powder Bed Fusion (L-PBF), also referred to as Selective Laser Melting (SLM), is one of the most popular and widely used metal additive manufacturing (AM) technology [1]. This process allows to build complex three dimensional (3D) parts by successive

* Corresponding author.

E-mail address: timothee.delacroix@outlook.fr (T. Delacroix).

addition of matter, and can be applied to a number of materials such as stainless steels, titanium alloys, aluminum alloys or nickel superalloys [2]. A thin layer of metallic powder (typically between 20 and 90 μm thick) is spread by a recoater upon a substrate plate, then one (or multiple) laser beam(s) melt the material selectively according to trajectories previously determined by the slicing of a digital 3D file. Rapid solidification of the molten metal, and successive repetition of these actions, layer upon layer, lead to the fabrication of near net-shape products with mechanical properties equivalent or superior to parts elaborated by conventional processes [3]. Manufacturing takes place in a chamber filled with a protective gas such as Ar or N_2 to prevent contamination of the melt pool, but the presence of residual oxygen in the gaseous atmosphere during fabrication cannot be avoided. Complex interactions between the laser and the powder can lead to imperfections and poor reproducibility in printed parts quality, with porosity, balling and cracks [4]. Extensive researches have been focused on understanding the origin of defects and optimizing L-PBF processing parameters to improve the parts properties [5–8]. The influence of the metallic powder is also a key challenge in metal AM regarding the printed parts quality and reproducibility [9].

Among the advantages offered by AM, the ability to reduce waste generation, by using the right amount of material to build the components, stands out when compared to conventional processes. During L-PBF process, only a small fraction of the powder is melted by the laser beam and solidified. To maximize the resource efficiency of this technology, there is a need to reuse the non-melted powder for future fabrications. However, it is known that intensive reuse of the powder, also called powder recycling, leads to a degradation of the particles attributes and can alter the properties of the final parts [10–15]. Successive recycling can lead to changes in particles morphology, chemical composition or microstructure. Evolution of feedstocks attributes is not necessarily linear with successive recycling and is not global, as powder degradation is mainly due to the presence of some altered particles among the recovered powder.

Characterization of powders can be performed *ex situ* on various instruments, but is often time-consuming. Another major issue is that, compared to the amounts used for printing, only small quantities of particles are generally analyzed. It would be interesting to improve this methodology by analyzing larger quantities and with more representative samples. This is in line with one high priority technical challenge to widespread adoption of AM, that is the development of process monitoring and control [2,16]. In L-PBF, the most commonly monitored target is the melt pool, for a better understanding of the process [17]. Research efforts have been focused on *in-situ* sensing of the size, shape and temperature of the molten pool, using thermal and optical sensors [18–21]. Image processing techniques are also used to detect material defects and anomalies on a layer-wise level [22]. Kleszczynski et al. [23] measured geometrical features to control the dimensional accuracy of the parts during the process. Jacobsmühlen et al. [24] were able to identify super-elevated area compared to the CAD model and to create mappings of these deviations. Abdelrahman et al. [25] presented a similar approach to detect potential parts defects and flaws. Monitoring of the powder bed slices before laser scanning is also implemented to detect local inhomogeneities that could have a detrimental effect on the final components quality. Recoating errors such as stripes in the powder bed parallel to the linear motion of the recoater were detected by Foster et al. [26] and Craeghs et al. [27]. Scime et al. [28–30] developed algorithms to classify multiple anomalies detected within a single powder bed image captured by the camera provided on the AM machine.

However, all these techniques and methodologies are performed with relatively low spatial resolution images to cover the

entire powder bed, and can therefore detect only relatively large anomalies. Pedersen et al. [31] proposed to use contact image sensors to scan the surface of the powder bed during the recoating procedure. This technique, with the use of sensors commonly found in flatbed document scanners, allows to capture the entire build area with individual powder particles resolution. Le and Seita [32] created a powder bed module with this linear optical sensor unit integrated on the recoater module. These sensors present a narrow depth-of-field, and the authors exploited out of focal plane zones in their mappings to determine variations in powder layer thickness. Surface roughness and surface particles density were also assessed with this method to study different powder batches and spreading strategies [33]. Using this kind of sensors mounted on the recoater offers the opportunity to perform *in situ* powder bed quality assessment regarding numerous features. To the authors' knowledge, there are no powder bed monitoring studies in the L-PBF literature featuring the use of color scans with very high spatial resolution in order to investigate particles oxidation. This feature can be a good indicator of the quality of the powder feedstocks. An increase of oxygen content in reused powder has been repeatedly observed in the literature for titanium alloys [34,35], aluminum alloys [36,37], but also stainless steels [14,38]. The presence of colored particles in the recycled feedstocks has also been observed [11,39]. Different colors can be observed on oxidized particles due to different oxide thicknesses displaying interference colors when exposed to white light [40].

The purpose of the present work is to assess the oxygen content of powder feedstocks by *in-line* scanning of powder bed layers. A new methodology is implemented on material stainless steel 316L (SS316L) to correlate the color of the oxidized particles to the powder oxygen content. To this end, for calibration purposes, several samples of virgin SS316L powder are oxidized in furnace with different combination of time and temperatures and their oxygen content is characterized by chemical analysis. Using an instrumented L-PBF platform with a customized recoater module including a contact image sensor, colored scans of powder beds are acquired at very high resolution (4800 dots-per-inch, dpi). This allows to derive a functional correlation between the oxygen concentration of those furnace-oxidized particles and the RGB (Red, Green, Blue) values of the scans. This correlation once modelled analytically, an inverse procedure can be used to determine the oxygen content of a powder bed made of unknown particles by means of a color scan. Different recycled powder samples from an L-PBF recycling study (up to 15 printing cycles without addition of any virgin powder) are scanned *in-situ* and analyzed with this methodology to investigate powder oxygen contents, by image analysis, and compared to *ex-situ* measurements.

2. Materials and methods

2.1. Methodology

As mentioned above, this work is based on a preliminary calibration, which allows the correlation between particles colors and oxygen content, with the ultimate objective of performing measurements of powders oxygen concentration by *in-line* scanning of powder bed layers. This calibration requires the following steps:

- (i) Oxidation of powder samples in furnace under different combinations of time and temperature;
- (ii) Oxygen content measurement of those oxidized powders by chemical analysis;
- (iii) Scan acquisition of those oxidized powder with determination of their RGB color values;

- (iv) Determination of a functional correlation between oxygen content and RGB color values.

Calibration and validation results will be presented separately. Section 3 details the steps (i-iv) introduced above. The results of the inverse procedure, that is the determination of the oxygen content of a given powder bed as a function of its RGB values in order to validate the methodology is presented in Section 4. Data will be obtained from several powder samples, that include recycled powders of different states collected from a previous study [41]. These powders were used, recovered, sieved and reused to produce 15 successive L-PBF fabrications on a Trumpf GmbH TruPrint 1000 printer without addition of virgin powder. Powder bed scans with virgin powder, 1-time recycled (R1), 5-times recycled (R5), 10-times recycled (R10) and 15-times recycled (R15) powders collected after the sieving step were acquired and analyzed. 'Artificially' degraded powder samples were also investigated with the present powder bed scanning technique, with mixes of virgin and furnace-oxidized powders at different fractions and oxygen contents. In all cases, the in-line measurements of oxygen content are compared to results obtained by ex-situ characterization using chemical analysis.

2.2. Feedstock material

This study was conducted with gas-atomized AISI 316L powder manufactured by Oerlikon Metco Europe GmbH. The powder is spherical, with a particle size distribution of 20–45 μm . The chemical composition is reported in Table 1, and fits within the range of the requirements of the ASTM F3184 norm [42] for SS316L in powder bed fusion.

2.3. Furnace oxidation

The samples of virgin SS316L powder to be used for the oxygen color correlation on the powder bed scanning setup were oxidized in a Nabertherm B180 furnace. Powder was disposed in alumina crucibles and heated in air at various combinations of durations and temperatures as listed in Table 2. Cooling also took place in air, at ambient temperature.

2.4. Powder characterization methods

Particles colors and morphology were observed by optical microscopy (OM, ZEISS Axio Imager 2). A JSM-7000F scanning electron microscope (SEM, JEOL) equipped with a field-emission gun was employed to generate high-resolutions micrographs. In addition, energy dispersive spectroscopy (EDS) was used to assess surface compositions of individual particles. The ex-situ measurement of powders oxygen content was performed by inert gas fusion with EMGA 820 AC analyzer from Horiba, with three to five measurements per sample.

2.5. Powder bed scanning setup

A customizable L-PBF test bench from the Processes and Engineering in Mechanics and Materials (PIMM – ENSAM) laboratory was used to integrate a scanner into the spreading unit of the machine. The schematic of the powder bed scanning setup is illustrated in Fig. 1. A 210 mm wide contact image sensor from a Canon

Table 2

Furnace temperatures and durations conditions for powder oxidation. Each duration is implemented at each temperature condition.

Temperature ($^{\circ}\text{C}$)	[300; 400; 500]
Duration (min)	[10; 30; 60; 90; 120]

Cano LiDE 220 flatbed scanner is mounted on two micrometric positioning tables that allow height adjustment and a slight correction of the inclination. The system is assembled on the recoater arm of the machine, which is controlled by an Aerotech servomotor.

The system allows to acquire colored scans of the entire powder bed area (\varnothing 150 mm) with a resolution up to 4800 dpi, using the commercial software of the flatbed scanner (Canon ScanGear). Such a resolution corresponds to a pixel size of $5.3 \mu\text{m} \times 5.3 \mu\text{m}$, requiring a displacement of the recoater arm at 0.16 mm/s. Speed calibration was performed to avoid any image distortion, by matching the recoater arm speed to the image acquisition rate of the scanner. Each data point is coded on 3 bytes, one per color channel, amounting to values between 0 and 255. Table 3 summarizes the spatial resolutions, scanning speeds and times, and image sizes for different image acquisition settings, all in colors.

It has to be noticed that the 4800 dpi colored scans, allowing individual powder particles resolution, result in an extremely slow scanning speed that is not representative of spreading speeds in L-PBF processing. Therefore, for this study, the powder layers were spread at a more common velocity of 50 mm/s, and the powder bed scans were captured at 0.16 mm/s on the way back. This issue of scan acquisition time will be discussed in Section 6. Nevertheless, it should be noted that such a long period of time is not limiting for the evaluation of the oxygen measurement technique. Fig. 2 shows an example of a powder bed scan displaying the entire build platform, with digital zooms of the raw image showing the high spatial resolution. To ensure a complete and homogeneous coverage of the whole area, three layers of 50 μm thickness were spread before acquiring the images of the powder beds to be used in the analyses. This sample is a 15-times recycled powder, and oxidized particles can be observed, with colors ranging from orange-brown to blue. Pre-processing (contrast, brightness) is automatically managed by the Canon ScanGear software. The raw data thus obtained is an input for the calibration with the determination of average colors, image analysis being carried out using ImageJ software and Python programming.

3. Calibration results

3.1. Powder oxidation in furnace

Fig. 3 represents the evolution of the oxygen content of furnace-oxidized powders as a function of heating time and temperature.

The three temperatures seem to follow parabolic oxidation kinetics, which is known for high temperature oxidation of alloys with the growth of an oxide film controlled by diffusional phenomena [43,44]. In the case of stainless steels, chromia (Cr_2O_3) oxide is expected to grow following the parabolic rate law given by Eq. (1) [45–47].

Table 1

Chemical composition of the virgin SS316L powder, in wt.%.

Element wt%	Fe Bal.	Cr 17.5	Ni 12.6	Mn 1.5	Mo 2.4	Si 0.04	N 0.07	C 0.02	P 0.002	S 0.001	O 0.048
----------------	------------	------------	------------	-----------	-----------	------------	-----------	-----------	------------	------------	------------

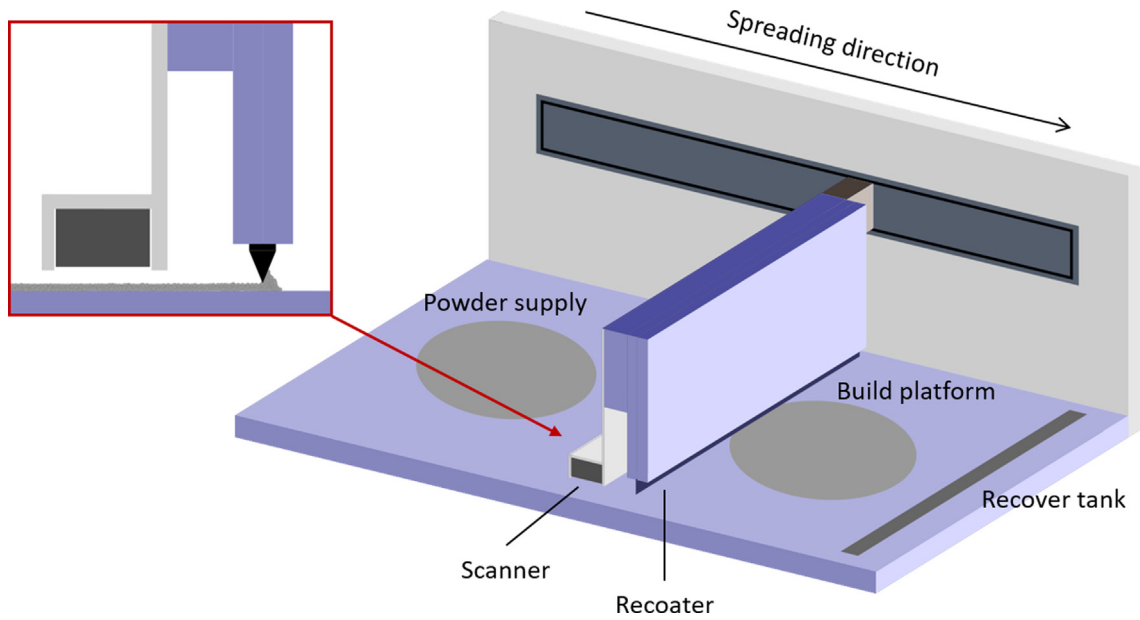


Fig. 1. Schematic of the powder bed scanning setup. Inset: detail on scanner attachment to recoating system.

Table 3

Resolutions, scanning speed and time, and image size for different colored image acquisition settings.

Resolution (dpi)	Spatial resolution (μm)	Scanned area (mm)	Scanning speed (mm/s)	Scanning time (s)	Image size (MB)
600	42.3×42.3	210×165	10	17	58
1200	21.2×21.2	210×165	2.52	65	233
2400	10.6×10.6	210×165	0.64	258	932
4800	5.3×5.3	210×165	0.16	1031	3729

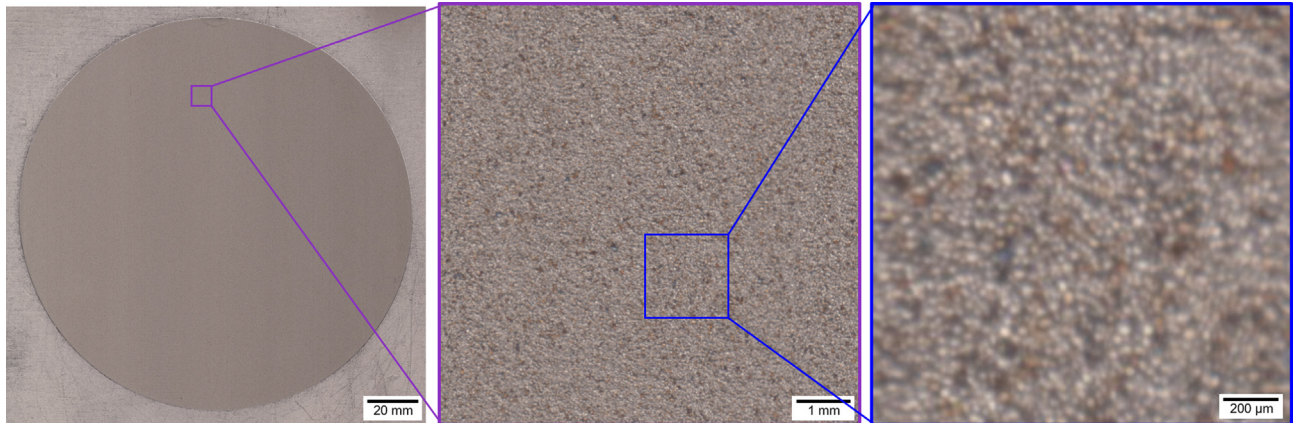


Fig. 2. Powder bed scan of recycled powder at 4800 dpi at increasing digital zooms of the raw image.

$$\left(\frac{\Delta m}{A}\right)^2 = k_p t + C \quad (1)$$

Where $\Delta m/A$ is the mass gain per unit area (in g.cm^{-2}), k_p is the parabolic oxidation rate constant (in $\text{g}^2.\text{cm}^{-4}.\text{s}^{-1}$), t is the duration of isothermal holding at the oxidation temperature (s), and C is another fit parameter. The determined k_p are equal to 1.9×10^{-16} , 1.6×10^{-15} , and $9.6 \times 10^{-15} \text{ g}^2.\text{cm}^{-4}.\text{s}^{-1}$ at 300, 400 and 500 °C respectively. An Arrhenius plot is represented Fig. 4, displaying the evolution of the parabolic oxidation constants of SS316L with the inverse temperature. The linear nature of this graph shows that all temperatures investigated in this study can be accounted for by a

temperature activated diffusional mechanism, following the Arrhenius law.

The k_p values agree with the literature for the growth of a protective chromia film, following the trend of oxidation rates determined at higher temperatures, such as by Hindam and Whittle [43], Felten [48] or Mortimer and Post [49] with k_p values ranging between 5×10^{-14} and $1.3 \times 10^{-13} \text{ g}^2.\text{cm}^{-4}.\text{s}^{-1}$ at 650 °C, or between 3×10^{-13} and $5 \times 10^{-12} \text{ g}^2.\text{cm}^{-4}.\text{s}^{-1}$ at 800 °C.

On a semi-quantitative basis, oxide scale thickness can be estimated on a representative SS316L powder particle, using the average particle radius of the powder ($r = 16.0 \mu\text{m}$) determined by laser

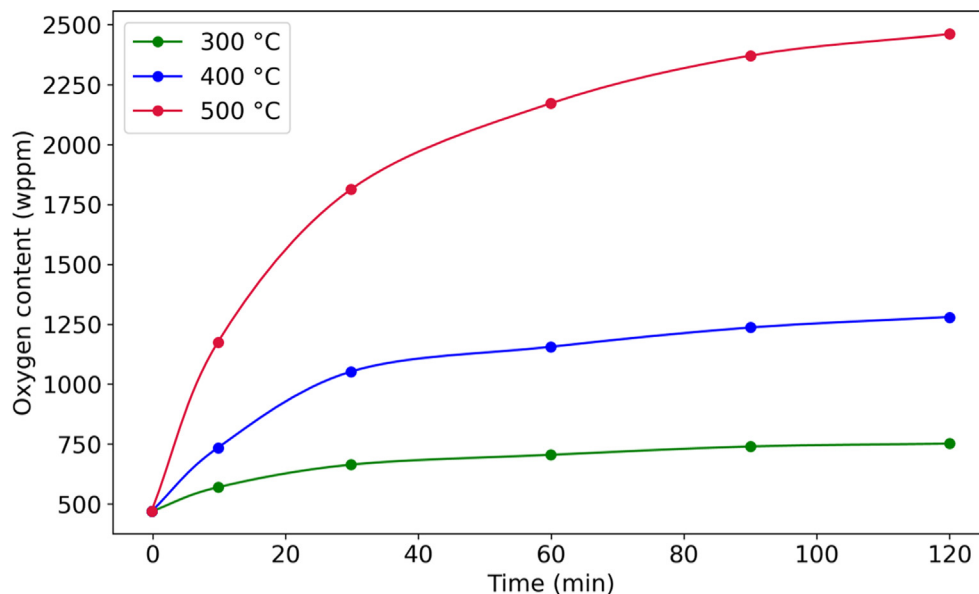


Fig. 3. Oxygen content of furnace-oxidized powders in function of heating time and temperature.

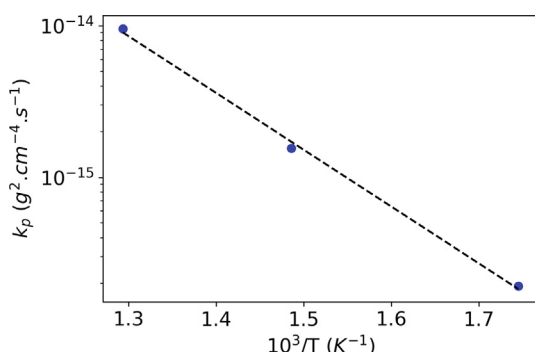


Fig. 4. Arrhenius diagram of the parabolic oxidation constants of SS316L between 300 °C and 500 °C.

granulometry, the powder oxygen content, and assuming that the oxide layer is uniform and consists of Cr_2O_3 . The approximation also includes the assumption that the initial oxygen and all oxygen pickup is present in the external oxide layer and does not exist as solid solution in the SS316L material. Calculations using Eq. (2) [39] yield to oxide thicknesses between 12 nm and 63 nm, which is in accordance with surface oxide thicknesses measured experimentally on stainless steel powders, or on oxidized samples [39,50,51].

$$t_{\text{oxide}} = \sqrt[3]{\frac{3m_o M(\text{Cr}_2\text{O}_3)}{4\pi\rho_{\text{Cr}_2\text{O}_3} S_o M(\text{O})}} + r^3 - r \quad (2)$$

Where t_{oxide} is the oxide thickness, m_o the mass of oxygen contained in the oxide layer, $M(\text{Cr}_2\text{O}_3)$ and $M(\text{O})$ the molar masses, respectively of chromia and oxygen, S_o the stoichiometry of oxygen in the oxide, $\rho_{\text{Cr}_2\text{O}_3}$ the density of the oxide, and r the average radius of the particle.

Different combination of heating-time and temperature can lead to a similar oxygen concentration, thus a similar oxide thickness. Optical microscopy observations of the oxidized powders reveal that regardless of the heating conditions, the colors

observed for a similar oxygen content are identical. As mentioned in the introduction, different colors are obtained because at various oxide layer thicknesses, due to the interferences of the light reflecting off the film/steel interface and the light reflecting off the top of the oxide surface (film/air interface) [40,52]. It is possible to sort the powders by increasing oxygen content, as illustrated with some oxidized samples in Fig. 5.

Correlation between OM and SEM observations were conducted in order to perform EDS point analysis on individual particles with known colors thanks to the OM images. The EDS results regarding the local oxygen concentrations confirmed the overall tendency observed on larger samples with global oxygen content values. Fig. 6a shows a set of oxidized particles observed by both OM and SEM, and Fig. 6b displays colored particles on which EDS analyses were performed, allowing to sort them by increasing oxygen. The classification of these individual particles is consistent with the sorting obtained from the oxygen contents measured by inert gas fusion.

3.2. Correlation of particles color with oxygen content

Furnace-oxidized powders were scanned using the powder bed scanning system. Raw images are then processed, with a cropping of the area of interest (the build plate) and the calculation of the average RGB color values for each scan. Fig. 7 presents examples of powder bed scans of oxidized samples and their corresponding average color.

A color can be specified as the combination of red, green and blue values, defining the intensity of each color parameter ranging between 0 and 255. The average values of R, G and B channels of all the scans capturing oxidized powder layers can be linked to the corresponding oxygen content of the samples, as represented in Fig. 8. Since what is measured is essentially the result of interference phenomena associated with the reflection from an incident white light, a qualitatively similar shape of the three curves is not unexpected.

In order to model the oxygen content as a function of the particles colors, a second-degree polynomial model was used, with the optimization of the coefficients to minimize the error. The function $O = f(R,G,B)$ reported in Eq. (3) fits the experimental values with a calculated correlation coefficient R^2 of 0.998.

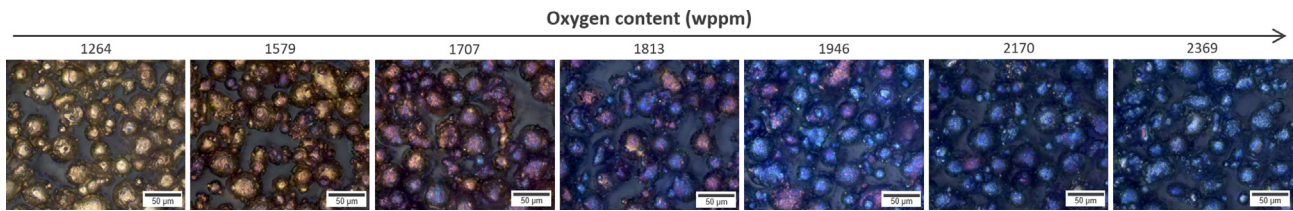


Fig. 5. Optical images of oxidized powders sorted by increasing oxygen content.

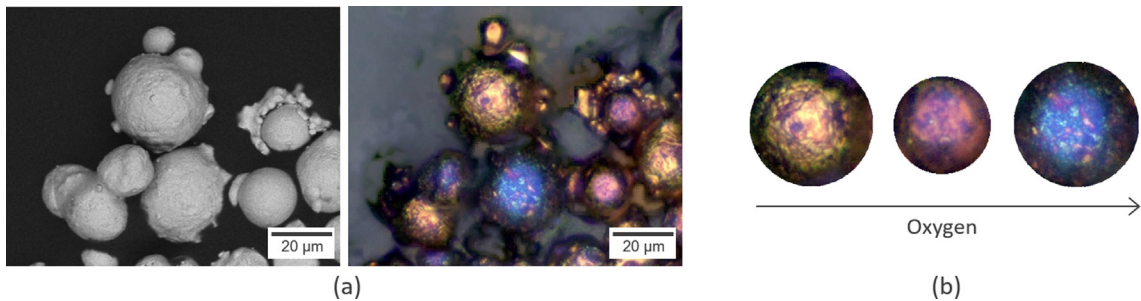


Fig. 6. (a) Correlation between SEM-BSE and OM on oxidized powder; (b) Colored particles sorted by increasing oxygen content assessed by EDS point analyses.

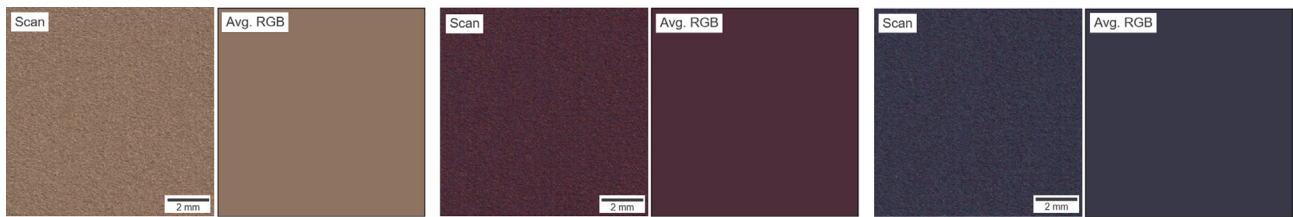


Fig. 7. Powder bed scans of oxidized powders along with their corresponding average color.

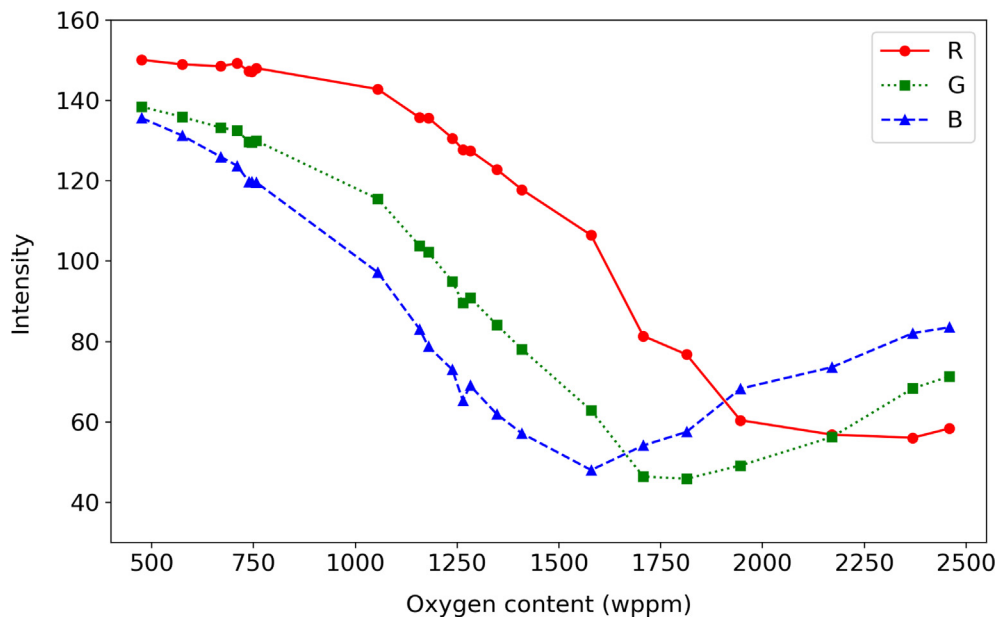


Fig. 8. Average values of Red (R), Green (G) and Blue (B) channels in the powder bed scans of oxidized powders in function the oxygen content. (For interpretation of the references to color in this figure legend, the reader is referred to the web version of this article.)

$$\begin{aligned}
 O = & 4036 - 18.26 * B - 0.4010 * B^2 + 45.54 * G + 0.363 * B \\
 & * G + 0.054 * G^2 - 49.05 * R + 0.3103 * B * R - 0.59 * G \\
 & * R + 0.2411 * R^2
 \end{aligned} \quad (3)$$

This oxygen prediction function allows to correlate the color of the SS316L powder bed to an oxygen concentration and to assess a possible degradation of powder bed layers by image analysis. A summary of the calibration methodology presented in this paper is schematized in Fig. 9.

4. Validation results

4.1. Measurement of recycled powder beds oxygen content

Several beds made of powders degraded through multiple L-PBF printing cycles and characterized in our previous work [41] were scanned and analyzed to check the validity of the method implemented in this work, that is the modeling of oxygen in function of RGB values (Eq. (3)). A remaining question pertains to the spatial scale at which the inverse procedure should be carried out. To this end, two methods were developed to measure the oxygen content in a powder bed scan. Fig. 10 shows these two different approaches. Method 1 consists in applying the prediction function to get the oxygen for each pixel of the scan, and then to calculate the average oxygen content of the bed by summation over all individual pixels. The second method calculates the average RGB in the scan and applies the prediction function with these three channel values as arguments. The second method is obviously much faster, but it could a priori lead to significantly different results, due to the nonlinear functional form of the polynomial function $O = f(R,G,B)$.

To illustrate matters, Fig. 11 presents powder bed scans of the virgin powder (R0) and the 15-times recycled state (R15). It is noticeable that the hue of the two scans observed globally are slightly different, with the powder bed with the R15 powder being darker/brown than the virgin powder which is gray. Digital zooms on the scans highlight particle to particle changes, and show the multitude of oxidized particles of different colors in the R15 scan.

Using the two methods presented in Fig. 10, powder beds oxygen content was measured for once recycled (R1), 5 times recycled (R5) in addition to R0 and R15 powder samples and compared to the ex-situ measurements determined by inert gas fusion (Fig. 12). A first positive result is that the scans values successfully follow the trend of increased oxygen concentration as the powder is more and more reused. The results are slightly higher with the scanning methods, up to 10–15 wppm, but still stay within the standard deviation of the chemical analysis values for some conditions. Another positive result is that the second method leads to results extremely close to those obtained with the first method (less than 5 wppm of difference). Hence, only the second method could be applied for future analysis of powder bed scans, as this approach provides almost instantaneous oxygen results (code execution of 70 ms for a 100 mm² area / 7 s for a 10 cm² area). The first method is nevertheless feasible and more rigorous. Besides, it opens a number of possibilities to assess oxygen content of a given powder bed at various spatial scales.

4.2. Repeatability analyses

Repeatability analyses were performed to study the potential dispersion that could occur between scans of different layers of an a priori identical powder batch. Fig. 13a shows the in-line oxygen content measurements for different powder bed layers of virgin powder, and Fig. 13b displays the results for different powder bed layers of R15 powder. The oxygen contents are consistent and always in close agreement with the value of inert gas fusion measurements. However, the highly recycled powder exhibits larger variations between different layers than the virgin powder, with standard deviations of 15 wppm and 6 wppm respectively, those values representing the standard deviation between single powder layers. This fluctuation can be explained by the fact that the recycled powder has a randomly distributed fraction of oxidized particles, and various powder spreadings can lead to physically and chemically different powder beds. On the other hand, virgin powder is much more uniform. These results suggest that

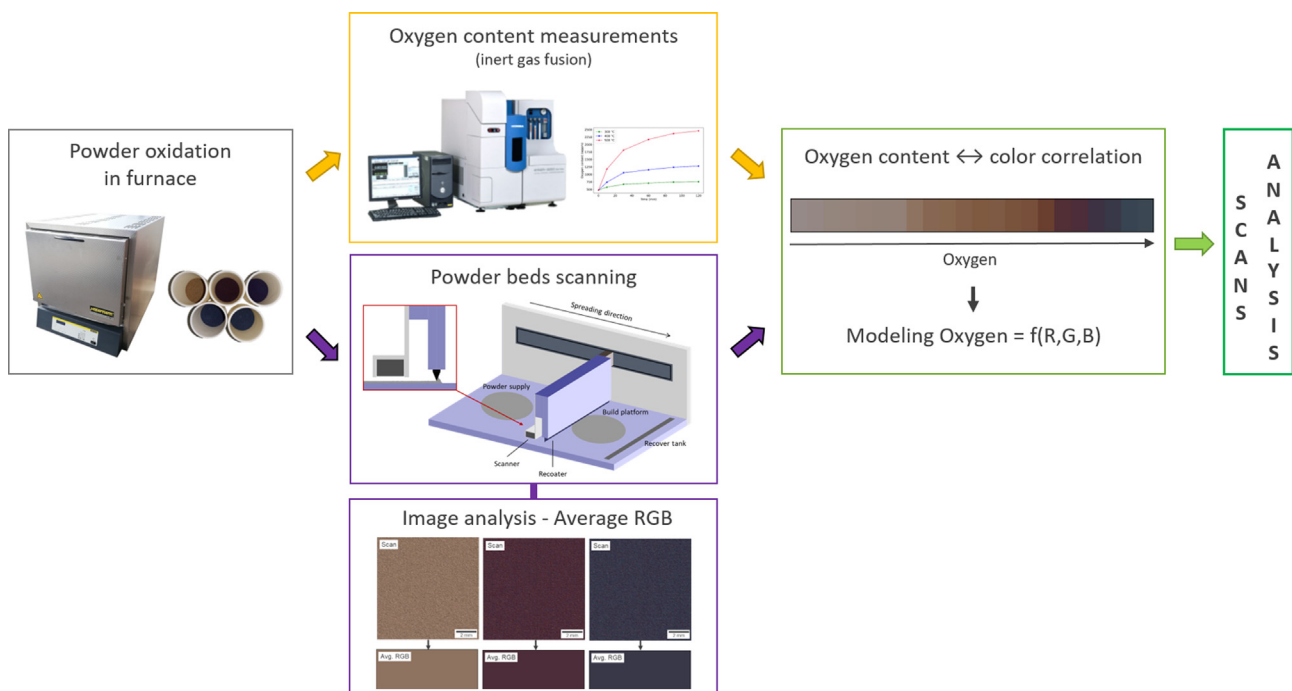


Fig. 9. Summary of the methodology developed for correlation between powder color and powder oxygen content.

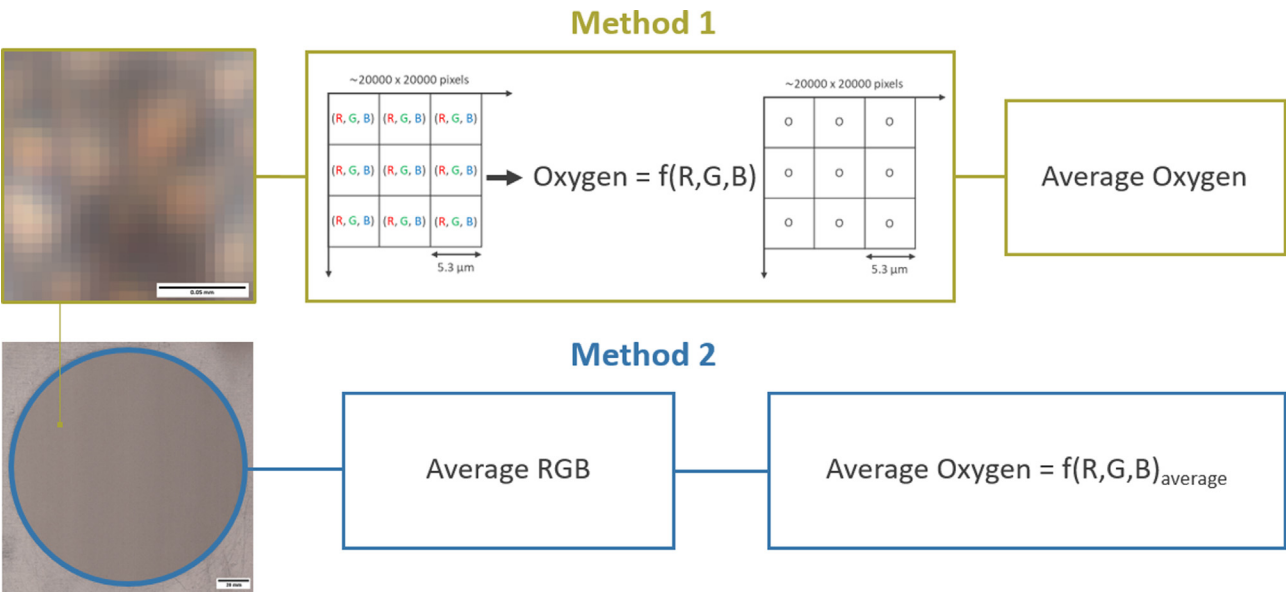


Fig. 10. Local (Method 1) and global (Method 2) procedures for oxygen content measurement in powder bed scans.

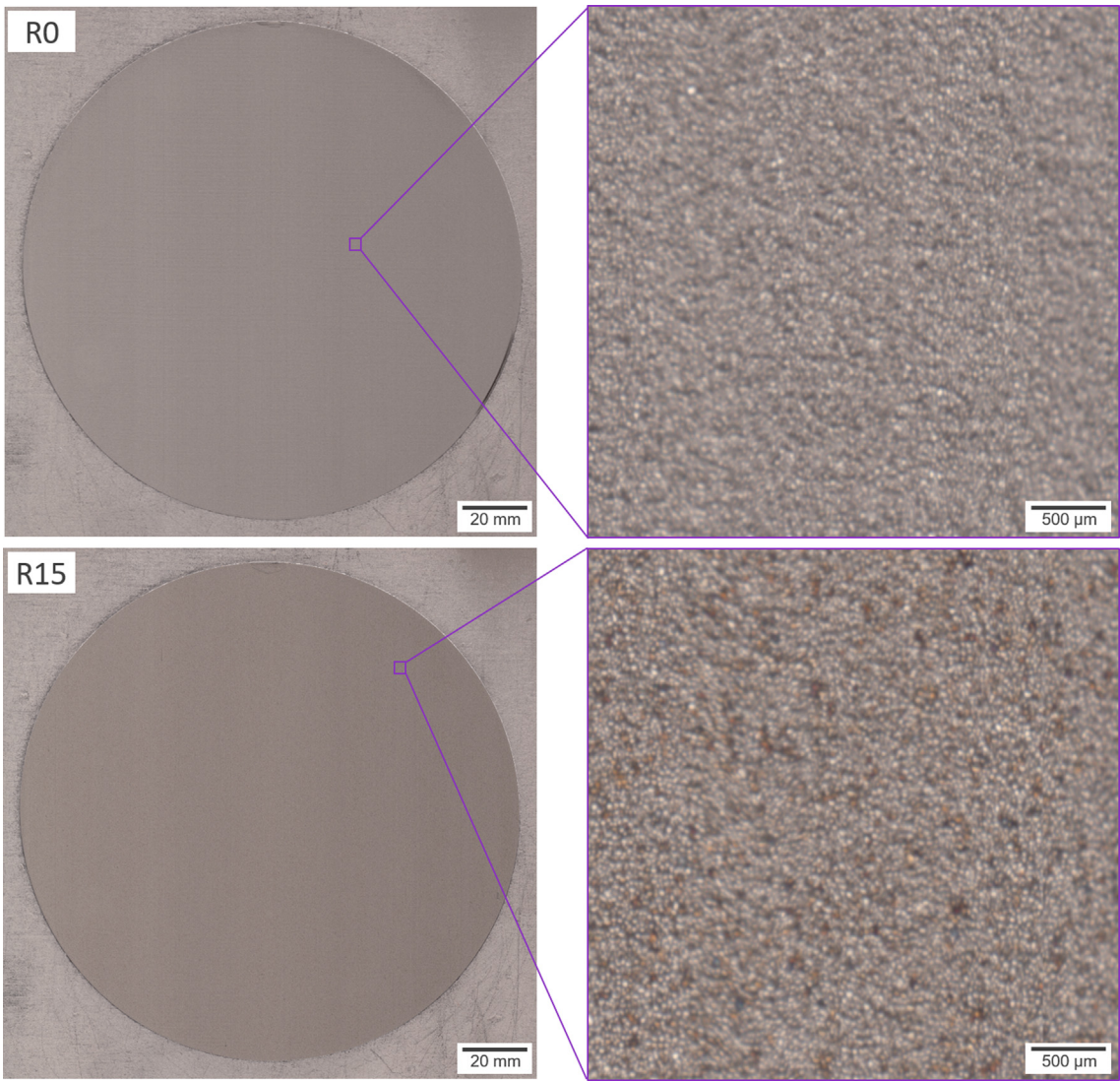


Fig. 11. Powder bed scans of virgin powder (R0) and 15-times recycled powder (R15), left, along with digital zooms, right.

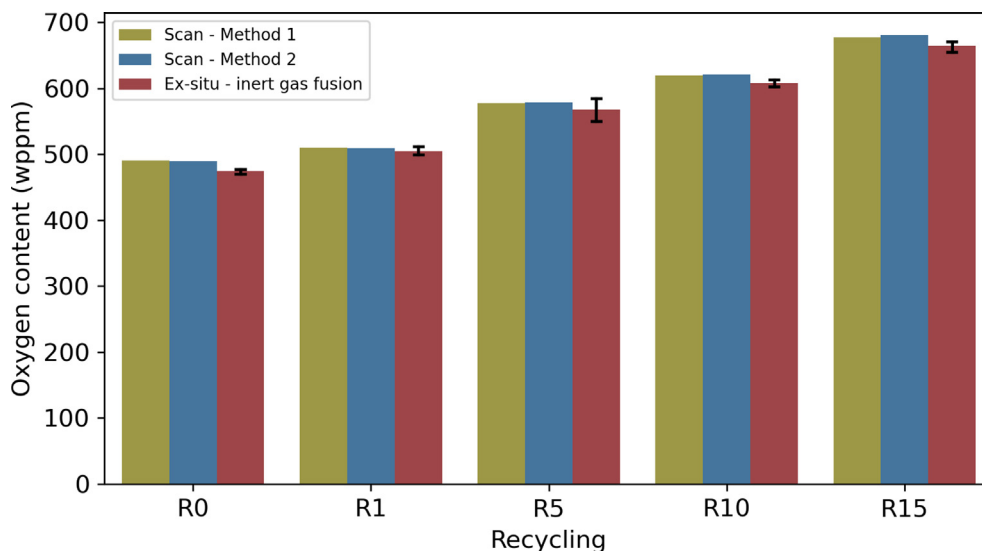


Fig. 12. Oxygen content of virgin and recycled powders measured by scan analysis and inert gas fusion.

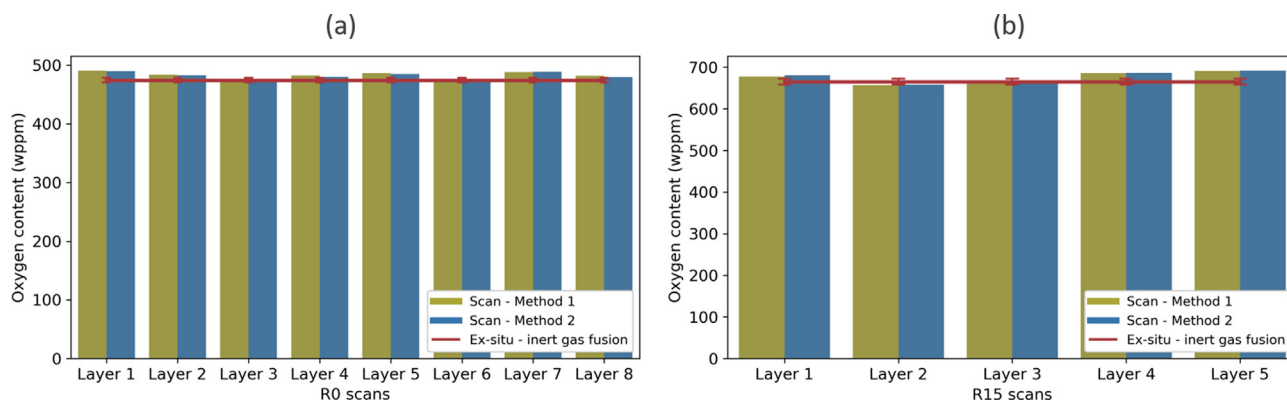


Fig. 13. Scans analyses repeatability with oxygen content measurements of different layers of (a) virgin powder and (b) R15 powder, compared to the corresponding inert gas fusion ex-situ measured concentration.

the proposed method may even make it possible to detect variations between different powder layers for heterogeneous batches, and thus determine the oxygen content in a more representative way than by conventional chemical analysis measurements.

Since the technique developed in the present work relies on the assessment of the color of the powder beds, optical artifacts can therefore distort the results. For instance, defects on the recoater, such as scratches will create lines in the direction of spreading. On the other hand, variations of the coating velocity could induce linear defects parallel to the movement of the recoater. Since such linear defects usually appear darker than the rest of the layer, they will consequently lead to an overestimation of the calculated oxygen content. In addition, the contact image sensors used in the powder bed scanning set-up present a really narrow depth-of-field, and some areas may appear a bit blurry due to layer height variations, which can also alter the results in terms of oxygen content.

The consistency of the results on the surface of the powder bed was also examined. A large square (106.8 cm²) inside the build platform was sliced into a 10 × 10 square grid and analyzed zone by zone. This allowed to draw oxygen content maps measured in each of these 100 zones. Fig. 14 presents the data acquisition procedure inside the powder bed along with the oxygen maps for virgin and R15 powder layers. The measurements presented here were obtained on each zone with the second image analysis

method (see Fig. 10). Whereas a good uniformity is observed along the direction of the recoater motion, significant variations are noticeable between the left and the right of the scans, i.e. transverse to the motion of the recoater. The bias is progressive over the width of the scan, with smaller values systematically reported on the left and larger ones on the right. A first potential explanation is related to a flatness defect of the build plate. The scans were acquired on large powder layers, after the spreading of several layers in order to replicate conditions that would occur during L-PBF processing, or at the end of a printing. However, the overall thickness of the powder bed still remained quite low, and unable to compensate a flatness defect of the build platform. Indeed, this planarity issue has been observed during the spreading of a single layer, with a thinner thickness on the left hand side. Another explanation for this spatial distortion could be a potential tilt of the scanner, the latter being mounted and adjusted manually with micrometric positioning tables. However, tests on images acquired with a desired inclination of the scanner also revealed the same distortion from left to right, although the tilt produced large areas of blur. Therefore, the hypothesis of the flatness defect of the plate remains the most plausible and leaves room for further improvement. Nevertheless, this spatial irregularity did not lead to distorted results thanks to its identification, and all the experiments (correlations, modeling and scan analyses) were replicated and conducted on a central area of the images. Moreover, even though

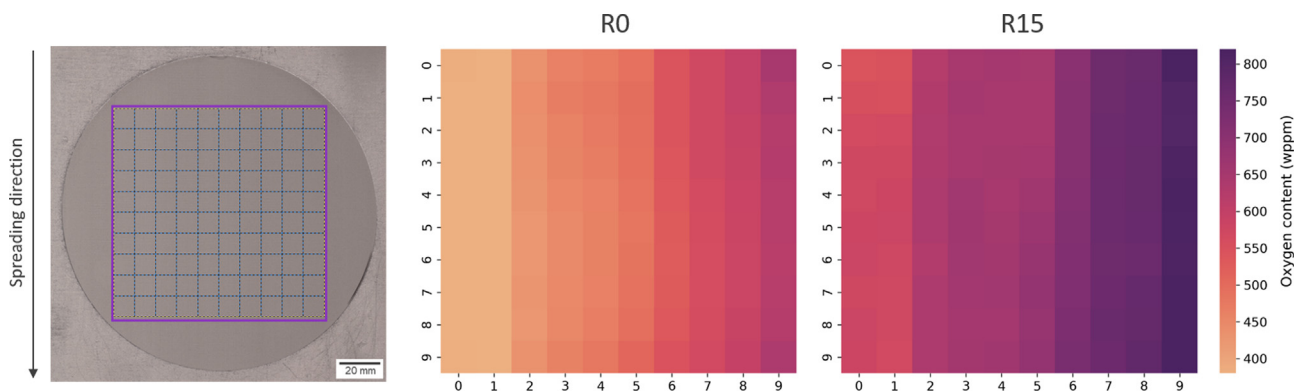


Fig. 14. Oxygen maps measured by scan analysis for virgin (R0) and R15 powders. A good uniformity is observed along the spreading direction, while a significant and progressive bias appears over the width of the scans, potentially due to a flatness defect of the substrate.

not *stricto sensu* related to the oxygen content, a positive byproduct of the methodology implemented in the frame of the present work is that it can assess other issues associated with the spreading of a powder bed.

4.3. Scan analyses of other degraded powder samples

4.3.1. Virgin powder mixed with furnace-oxidized powders

'Artificially' degraded powder samples were also analyzed, with the scanning of mixes of fresh powder containing different fractions of furnace-oxidized powders (5 and 10 wt%) with different oxygen levels L1 and L2 (Fig. 15). For information, these oxidized powders were obtained after heating at 500 °C for 10 and 90 min respectively. The theoretical values in the graph represent the expected oxygen concentration of the powder mixes based on the mass fractions and oxygen contents of the two constituents. Inert gas fusion measurements of the four samples are in almost perfect agreement with the theoretically calculated values. As for the results of the scanning procedure, both methods slightly overestimate the values compared to those of the chemical analysis. The trends are still respected, and the results from the two methods are once again almost identical. For a given fraction of oxidized particles in the mixes, the overestimation is more pronounced for L1 samples. The latter are composed of light orange particles, while L2 samples contain blue particles.

A tentative explanation for the difference between L1 and L2 batches is associated to the observation that quite generally the edges of colored particles appear darker on the acquired images, potentially leading to an overestimation of the oxygen level. L2 oxidized particles being already quite dark, the edge effect is not as pronounced, with less color variations, which could explain the smaller differences as compared to the L1 mixes. Moreover, for a given batch, the difference is more important for the samples with 10 % of colored particles. Increasing the number of colored particles reinforces the edge effect and therefore results in larger divergences.

4.3.2. Un-sieved powder and sieved residues

Some other samples of powders recovered after 1-PBF printing were also analyzed, to enlarge the collected database and to further validate the concept. Another R1 powder (collected after one printing cycle) was assessed, but whereas up to now all recycled powders had been submitted to a sieving procedure through a 50 µm mesh, un-sieved powders were also tested. The difference with standard R1 powder is that un-sieved powders contain large spatter particles, which slightly increases the oxygen content of the batch compared to samples after screening (535 ± 11 wppm versus 519 ± 12 wppm, measured by inert gas fusion). Scan analysis reliably predicts the oxygen concentrations, with values of 540 wppm and 516 wppm respectively, using the second method shown in Fig. 10.

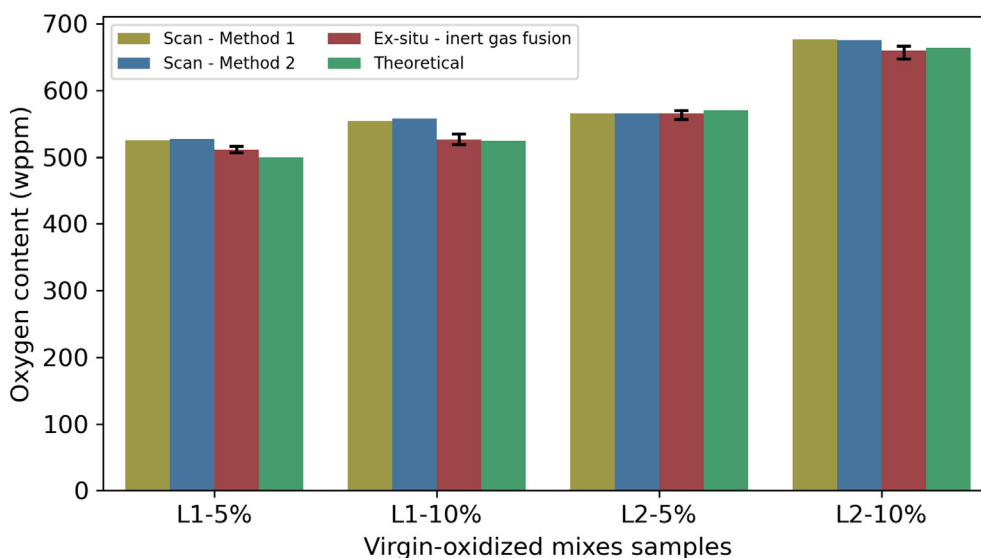


Fig. 15. Oxygen content of mixes of furnace-oxidized powders and virgin powder measured by scan analysis and inert gas fusion.

Powder beds consisting only of sieved residues from various L-PBF prints were also tested. The scanning method calculates an average oxygen of around 1400 wppm, whereas chemical analysis estimates 1600 wppm. Even though the difference in terms of oxygen content is much higher than in all previously reported cases, the in-line method is once again quite consistent, even with these unconventional really large particles with extremely high oxygen contents. The underestimation observed can come from two factors, related to the unconventional characteristics of the sieved residues. First, these particles are clearly not optimal for powder spreading, with the presence of satellites, low sphericity and large sizes. The poor spreading results in dragged particles leaving areas without powder, which minimizes the oxygen content due to the grey color of the build plate. Secondly, sieved residues contain melt pool ejecta, which are known to exhibit oxide nodules on their surface with the selective oxidation of Mn and Si for stainless steel powders [11,37,53]. Those spatter particles and nodules are not necessarily colored, therefore this oxidation will not be taken into account by the image analysis method. A last point to be mentioned is that the oxygen content of some sieved residue particles may be above the highest tested range for the derivation of the correlation. Nevertheless, with all these limitations in mind, it is remarkable that the scanning procedure can provide a decent estimate of the oxygen content for powder beds way out of the L-PBF standard. Besides, it is important to note that for commonly recovered un-sieved powders having typical fractions of spatter blended with the other particles, the scanning method remains quite accurate.

5. Conclusion

In this work, a new methodology was developed to measure the oxygen content of powder beds by in-line scanning of spread powder layers. The layer-by-layer fabrication of parts typical of AM and L-PBF offers the possibility to monitor material quality at a layer-wise level. An L-PBF machine was customized to integrate a scanner into the spreading unit of the machine. This system allowed to acquire in-line colored scans with high spatial resolution (4800 dpi) capturing the entire powder bed area.

The approach detailed in the present paper is based on a preliminary calibration, in order to correlate the color of the particles to their oxygen content. The methodology includes the oxidation in furnace of powder batches at 300 °C, 400 °C and 500 °C, from 10 to 120 min, followed by the measurement of the corresponding oxygen contents by chemical analysis. Powder bed scanning of those furnace-oxidized powders then enables to determine the average RGB values of the scans and to model the oxygen content as a function of the three color channel levels.

This method allows to accurately predict the oxygen concentration in a powder bed layer, after powder bed scanning and a fast image analysis consisting only of calculating the average RGB colors and applying the oxygen prediction function. Several case studies were implemented with scan analysis of recycled powder samples at different degradation states. The determined powder beds oxygen contents were demonstrated to be in very good agreements with ex-situ measurements performed by inert gas fusion.

In-line measurement offers the possibility to control the quality of the powder bed on larger quantities that are directly representative of the L-PBF feedstock. Scanning of several layers of 15 times recycled powder allowed to detect variations within a same batch. The present method thus appears as an interesting alternative to address the issue of oxygen content at the layer scale, thus complementing conventional chemical analyses at either larger or lower dimensional scales.

6. Future work

The relative simplicity of the method opens perspectives for automation and in-situ development of this methodology. However, a limiting factor is the long acquisition time of the scan to provide such high spatial resolution. The use of another scanner could slightly improve the speed of acquisition, but no order of magnitude gain can be expected. To circumvent the issue, one could think of carrying out the powder bed scans only at some key time locations of the fabrication, namely at the beginning of the L-PBF process, during the injection of the inert gas in the build chamber, and at the end of the process while the printed parts are cooling down. These operations would not alter the productivity of the process and would ensure quality control. Moreover, some L-PBF machines now operate in closed loops, making it otherwise rather difficult to track changes in particles attributes. In addition, monitoring the oxygen content of the feedstock could help in predicting certain properties of the printed parts [54,55].

The feasibility and repeatability of the results could also be evaluated by acquiring lower resolution scans, which would allow a very significant time gain. Given the completely satisfactory results of the second scan analysis method, based on the averaging of the colors on the powder bed before applying the oxygen prediction function, one could assume that a lower resolution acquisition (thus larger pixel size) already performs a similar averaging during the image acquisition and could result in reliable outcomes.

Other types of more sophisticated image analysis could also be considered to improve the monitoring process reliability. For example, particle detection could be implemented in order to remove the edges and only assess the central pixels of each particle. It should be kept in mind that for consistency purposes, any change of image analysis methodology would need to be carried out during the calibration leading to the correlation function as well.

The proposed methodology was developed with stainless steel 316L powders, with the identification of a correlation function $O = f(R,G,B)$ corresponding to colors of SS316L oxidized particles. This approach could be easily transposed to other materials, such as titanium alloys that are also known to exhibit colored oxidized particles. However, since the correlation function is expected to depend on the optical indices of the oxide layers, a calibration procedure for each new species investigated would certainly be necessary.

Still on the perspectives standpoint, the database from furnace oxidation experiments could be extended to other combination of heating temperature and exposure time. These studies could be coupled with further theoretical modeling of the oxidation phenomena, with the ultimate objective of predicting oxygen pickup in given process conditions. One could also think of theoretically predict particles coloration from the oxide films thicknesses and their optical properties. This model and further investigations would allow to better understand the oxidation mechanisms of powders occurring during the L-PBF process.

With the knowledge of the potential conditions leading to a given oxidation behavior, it would be interesting to investigate the impact of other L-PBF processing parameters on powder degradation, such as the influence of heating plate temperature, overall parts fraction in the powder heap and fabrication height, or build chamber atmosphere. Better understanding of powder degradation, combined with better control of powders attributes will help to increase material yield and process robustness.

CRedit authorship contribution statement

Timothée Delacroix: Methodology, Validation, Investigation, Formal analysis, Software, Writing – original draft, Writing – review & editing, Visualization. **Fernando Lomello:** Conceptualiza-

tion, Writing – review & editing, Supervision. **Frédéric Schuster:** Conceptualization, Funding acquisition. **Hicham Maskrot:** Resources, Project administration. **Vincent Jacquier:** Formal analysis, Software. **Pierre Lapouge:** Investigation, Methodology. **Frédéric Coste:** Investigation, Methodology. **Jean-Paul Garandet:** Conceptualization, Formal analysis, Writing – review & editing, Supervision.

Declaration of Competing Interest

The authors declare that they have no known competing financial interests or personal relationships that could have appeared to influence the work reported in this paper.

Acknowledgments

The authors gratefully acknowledge the technical and financial support provided by the CEA Cross-Cutting Program on Materials and Processes Skills, France.

Data availability

The raw/processed data required to reproduce these findings cannot be shared at this time as the data also forms part of an ongoing study.

References

- [1] H. Fayazfar, M. Salarian, A. Rogalsky, D. Sarker, P. Russo, V. Paserin, E. Toyserkani, A critical review of powder-based additive manufacturing of ferrous alloys: Process parameters, microstructure and mechanical properties, *Mater. Des.* 144 (2018) 98–128, <https://doi.org/10.1016/j.matdes.2018.02.018>.
- [2] W.E. Frazier, Metal Additive Manufacturing: A Review, *J. Mater. Eng. Perform.* 23 (2014) 1917–1928, <https://doi.org/10.1007/s11665-014-0958-z>.
- [3] Y.M. Wang, T. Voisin, J.T. McKeown, J. Ye, N.P. Calta, Z. Li, Z. Zeng, Y. Zhang, W. Chen, T.T. Roehling, R.T. Ott, M.K. Santala, P.J. Depond, M.J. Matthews, A.V. Hamza, T. Zhu, Additively manufactured hierarchical stainless steels with high strength and ductility, *Nat. Mater.* 17 (2018) 63–71, <https://doi.org/10.1038/nmat5021>.
- [4] T. DebRoy, H.L. Wei, J.S. Zuback, T. Mukherjee, J.W. Elmer, J.O. Milewski, A.M. Beese, A. Wilson-Heid, A. De, W. Zhang, Additive manufacturing of metallic components – Process, structure and properties, *Progress Mater. Sci.* 92 (2018) 112–224, <https://doi.org/10.1016/j.pmatsci.2017.10.001>.
- [5] E. Liverani, S. Toschi, L. Ceschini, A. Fortunato, Effect of selective laser melting (SLM) process parameters on microstructure and mechanical properties of 316L austenitic stainless steel, *J. Mater. Process. Technol.* 249 (2017) 255–263, <https://doi.org/10.1016/j.jmatprotec.2017.05.042>.
- [6] N.T. Aboulkhair, N.M. Everitt, I. Ashcroft, C. Tuck, Reducing porosity in AlSi10Mg parts processed by selective laser melting, *Addit. Manuf.* 1–4 (2014) 77–86, <https://doi.org/10.1016/j.addma.2014.08.001>.
- [7] M.L. Montero-Sistiaga, M. Godino-Martinez, K. Boschmans, J.-P. Kruth, J. Van Humbeeck, K. Vanmeensel, Microstructure evolution of 316L produced by HP-SLM (high power selective laser melting), *Addit. Manuf.* 23 (2018) 402–410, <https://doi.org/10.1016/j.addma.2018.08.028>.
- [8] M. Yakout, M.A. Elbestawi, S.C. Veldhuis, Density and mechanical properties in selective laser melting of Invar 36 and stainless steel 316L, *J. Mater. Process. Technol.* 266 (2019) 397–420, <https://doi.org/10.1016/j.jmatprotec.2018.11.006>.
- [9] L. Dowling, J. Kennedy, S. O'Shaughnessy, D. Trimble, A review of critical repeatability and reproducibility issues in powder bed fusion, *Mater. Des.* 186 (2020), <https://doi.org/10.1016/j.matdes.2019.108346>.
- [10] F.C. Pinto, I.R. Souza Filho, M.J.R. Sandim, H.R.Z. Sandim, Defects in parts manufactured by selective laser melting caused by δ -ferrite in reused 316L steel powder feedstock, *Addit. Manuf.* 31 (2020), <https://doi.org/10.1016/j.addma.2019.100979>.
- [11] M.J. Heiden, L.A. Deibler, J.M. Rodelas, J.R. Koepke, D.J. Tung, D.J. Saiz, B.H. Jared, Evolution of 316L stainless steel feedstock due to laser powder bed fusion process, *Add. Manuf.* 25 (2019) 84–103, <https://doi.org/10.1016/j.addma.2018.10.019>.
- [12] V. Seyda, N. Kaufmann, C. Emmelmann, Investigation of Aging Processes of Ti-6Al-4 V Powder Material in Laser Melting, *Phys. Proc.* 39 (2012) 425–431, <https://doi.org/10.1016/j.phpro.2012.10.057>.
- [13] F. Ahmed, U. Ali, D. Sarker, E. Marzbanrad, K. Choi, Y. Mahmoodkhani, E. Toyserkani, Study of powder recycling and its effect on printed parts during laser powder-bed fusion of 17–4 PH stainless steel, *J. Mater. Process. Technol.* (2019), <https://doi.org/10.1016/j.jmatprotec.2019.116522>.
- [14] A.T. Sutton, C.S. Kriewall, S. Karnati, M.C. Leu, J.W. Newkirk, Characterization of AISI 304L stainless steel powder recycled in the laser powder-bed fusion process, *Addit. Manuf.* 32 (2020), <https://doi.org/10.1016/j.addma.2019.100981>.
- [15] A.T. Sutton, C.S. Kriewall, S. Karnati, M.C. Leu, J.W. Newkirk, W. Everhart, B. Brown, Evolution of AISI 304L stainless steel part properties due to powder recycling in laser powder-bed fusion, *Addit. Manuf.* 36 (2020), <https://doi.org/10.1016/j.addma.2020.101439>.
- [16] Y. Huang, M.C. Leu, J. Mazumder, A. Donmez, Additive Manufacturing: Current State, Future Potential, Gaps and Needs, and Recommendations, *J. Manuf. Sci. Eng.* 137 (2015), <https://doi.org/10.1115/1.4028725>.
- [17] M. Grasso, B.M. Colosimo, Process defects and in situ monitoring methods in metal powder bed fusion: a review, *Meas. Sci. Technol.* 28 (2017), <https://doi.org/10.1088/1361-6501/aa5c4f>.
- [18] S. Clijsters, T. Craeghs, S. Bults, K. Kempen, J.-P. Kruth, In situ quality control of the selective laser melting process using a high-speed, real-time melt pool monitoring system, *Int. J. Adv. Manuf. Technol.* 75 (2014) 1089–1101, <https://doi.org/10.1007/s00170-014-6214-8>.
- [19] P. Lott, H. Schleifenbaum, W. Meiners, K. Wissenbach, C. Hinke, J. Bültmann, Design of an Optical system for the In Situ Process Monitoring of Selective Laser Melting (SLM), *Phys. Procedia* 12 (2011) 683–690, <https://doi.org/10.1016/j.phpro.2011.03.085>.
- [20] M. Doubenskaia, M. Pavlov, Y. Chivel, Optical System for On-Line Monitoring and Temperature Control in Selective Laser Melting Technology, *Key Eng. Mater.* 437 (2010) 458–461, <https://doi.org/10.4028/www.scientific.net/KEM.437.458>.
- [21] J.A. Kanko, A.P. Sibley, J.M. Fraser, In situ morphology-based defect detection of selective laser melting through inline coherent imaging, *J. Mater. Process. Technol.* 231 (2016) 488–500, <https://doi.org/10.1016/j.jmatprotec.2015.12.024>.
- [22] S.K. Everton, M. Hirsch, P. Stravroulakis, R.K. Leach, A.T. Clare, Review of in-situ process monitoring and in-situ metrology for metal additive manufacturing, *Mater. Des.* 95 (2016) 431–445, <https://doi.org/10.1016/j.matdes.2016.01.099>.
- [23] S. Kleszczynski, J. zur Jacobsmühlen, G. Witt, J. Sehr, Error detection in laser beam melting systems by high resolution imaging, in: *Proceedings of the Twenty Third Annual International Solid Freeform Fabrication Symposium*, 2012.
- [24] J. zur Jacobsmühlen, S. Kleszczynski, D. Schneider, G. Witt, High resolution imaging for inspection of Laser Beam Melting systems, 2013 IEEE International Instrumentation and Measurement Technology Conference (I2MTC), (2013). 10.1109/I2MTC.2013.6555507.
- [25] M. Abdelrahman, E.W. Reutzel, A.R. Nassar, T.L. Starr, Flaw detection in powder bed fusion using optical imaging, *Addit. Manuf.* 15 (2017) 1–11, <https://doi.org/10.1016/j.addma.2017.02.001>.
- [26] K.B. Foster, W.E. Reutzel, R.A. Nassar, T.B. Hall, W.S. Brown, C.J. Dickman, Optical, layerwise monitoring of powder bed fusion, *Solid Free. Fabr. Symp. Proc.* (2015) 295–307.
- [27] T. Craeghs, F. Bechmann, S. Berumen, J.-P. Kruth, Feedback control of Layerwise Laser Melting using optical sensors, *Phys. Procedia* 5 (2010) 505–514, <https://doi.org/10.1016/j.phpro.2010.08.078>.
- [28] L. Scime, J. Beuth, Anomaly detection and classification in a laser powder bed additive manufacturing process using a trained computer vision algorithm, *Addit. Manuf.* 19 (2018) 114–126, <https://doi.org/10.1016/j.addma.2017.11.009>.
- [29] L. Scime, J. Beuth, A multi-scale convolutional neural network for autonomous anomaly detection and classification in a laser powder bed fusion additive manufacturing process, *Addit. Manuf.* 24 (2018) 273–286, <https://doi.org/10.1016/j.addma.2018.09.034>.
- [30] L. Scime, D. Siddel, S. Baird, V. Paquit, Layer-wise anomaly detection and classification for powder bed additive manufacturing processes: A machine-agnostic algorithm for real-time pixel-wise semantic segmentation, *Addit. Manuf.* 36 (2020), <https://doi.org/10.1016/j.addma.2020.101453>.
- [31] D.B. Pedersen, E.R. Eiriksson, H. Aanæs, H.N. Hansen, In-Situ Monitoring in Additive Manufacturing Using Contact Image Sensors: ASPE Summer Topical Meeting 2016, in: *Proceedings of the ASPE/Euspen 2016 Summer Topical Meeting on Dimensional Accuracy and Surface Finish in Additive Manufacturing*, 2016, pp. 114–118.
- [32] L. Tan Phuc, M. Seita, A high-resolution and large field-of-view scanner for inline characterization of powder bed defects during additive manufacturing, *Mater. Des.* 164 (2019), <https://doi.org/10.1016/j.matdes.2018.107562>.
- [33] T.-P. Le, X. Wang, K.P. Davidson, J.E. Fronda, M. Seita, Experimental analysis of powder layer quality as a function of feedstock and recoating strategies, *Addit. Manuf.* 39 (2021), <https://doi.org/10.1016/j.addma.2021.101890>.
- [34] O.A. Quintana, J. Alvarez, R. Mcmillan, W. Tong, C. Tomonto, Effects of Reusing Ti-6Al-4V Powder in a Selective Laser Melting Additive System Operated in an Industrial Setting, *JOM* 70 (2018) 1863–1869, <https://doi.org/10.1007/s11837-018-3011-0>.
- [35] H.P. Tang, M. Qian, N. Liu, X.Z. Zhang, G.Y. Yang, J. Wang, Effect of Powder Reuse Times on Additive Manufacturing of Ti-6Al-4V by Selective Electron Beam Melting, *JOM* 67 (2015) 555–563, <https://doi.org/10.1007/s11837-015-1300-4>.
- [36] L. Cordova, M. Campos, T. Tinga, Revealing the Effects of Powder Reuse for Selective Laser Melting by Powder Characterization, *JOM* 71 (2019) 1062–1072, <https://doi.org/10.1007/s11837-018-3305-2>.

- [37] M. Simonelli, C. Tuck, N.T. Aboulkhair, I. Maskery, I. Ashcroft, R.D. Wildman, R. Hague, A Study on the Laser Spatter and the Oxidation Reactions During Selective Laser Melting of 316L Stainless Steel, Al-Si10-Mg, and Ti-6Al-4V, *Metall. Mat. Trans. A*. 46 (2015) 3842–3851, <https://doi.org/10.1007/s11661-015-2882-8>.
- [38] N.E. Gorji, R. O'Connor, A. Mussatto, M. Snelgrove, P.G.M. González, D. Brabazon, Recyclability of stainless steel (316 L) powder within the additive manufacturing process, *Materialia*. 8 (2019), <https://doi.org/10.1016/j.mtla.2019.100489> 100489.
- [39] D. Galicki, F. List, S.S. Babu, A. Plotkowski, H.M. Meyer, R. Seals, C. Hayes, Localized Changes of Stainless Steel Powder Characteristics During Selective Laser Melting Additive Manufacturing, *Metall. Mat. Trans. A*. 50 (2019) 1582–1605, <https://doi.org/10.1007/s11661-018-5072-7>.
- [40] J. Ki Leuk Lai, K. Ho Lo, C. Hung Shek, (eds.), Chapter 12 - Colouration of Stainless Steels, in: *Stainless Steels: An Introduction and Their Recent Developments*, BENTHAM SCIENCE PUBLISHERS, 2012: p. 151. 10.2174/97816080530561120101.
- [41] T. Delacroix, F. Lomello, F. Schuster, H. Maskrot, J.-P. Garandet, Influence of powder recycling on 316L stainless steel feedstocks and printed parts in laser powder bed fusion, *Addit. Manuf.* 50 (2022), <https://doi.org/10.1016/j.addma.2021.102553> 102553.
- [42] ASTM F3184-16, Standard Specification for Additive Manufacturing Stainless Steel Alloy (UNS S31603) with Powder Bed Fusion, ASTM International, West Conshohocken, PA, 2016. 10.1520/F3184-16.
- [43] H. Hindam, D.P. Whittle, Microstructure, adhesion and growth kinetics of protective scales on metals and alloys, *Oxid. Met.* 18 (1982) 245–284, <https://doi.org/10.1007/BF00656571>.
- [44] P. Moulin, A.M. Huntz, P. Lacombe, Influence des phenomenes diffusionnels sur le mecanisme d'oxydation des alliages NiCr, *Acta Metall.* 28 (1980) 745–756, [https://doi.org/10.1016/0001-6160\(80\)90152-2](https://doi.org/10.1016/0001-6160(80)90152-2).
- [45] A.M. Huntz, A. Reckmann, C. Haut, C. Sév  rac, M. Herbst, F.C.T. Resende, A.C.S. Sabioni, Oxidation of AISI 304 and AISI 439 stainless steels, *Mater. Sci. Eng. A* 447 (2007) 266–276, <https://doi.org/10.1016/j.msea.2006.10.022>.
- [46] A.C.S. Sabioni, R.P.B. Ramos, V. Ji, F. Jomard, Oxygen Diffusion Study in Oxidation Films of the AISI 304 Austenitic Stainless Steel, *Defect and Diffusion, Forum* 323–325 (2012) 345–351, <https://doi.org/10.4028/www.scientific.net/DDF.323-325.345>.
- [47] J. Karczewski, T. Brylewski, T. Miruszewski, K.B. Andersen, P.Z. Jasinski, S. Molin, High-temperature kinetics study of 430L steel powder oxidized in air at 600–850 °C, *Corros. Sci.* 149 (2019) 100–107, <https://doi.org/10.1016/j.corsci.2019.01.005>.
- [48] E.J. Felten, High-Temperature Oxidation of Fe-Cr Base Alloys with Particular Reference to Fe-Cr-Y Alloys, *J. Electrochem. Soc.* 108 (1961) 490, <https://doi.org/10.1149/1.2428122>.
- [49] D. Mortimer, M.L. Post, The oxidation of Cr and an Fe-50% Cr alloy, *Corros. Sci.* 8 (1968) 499–512, [https://doi.org/10.1016/S0010-938X\(68\)80005-8](https://doi.org/10.1016/S0010-938X(68)80005-8).
- [50] D. Riabov, E. Hryha, M. Rashidi, S. Bengtsson, L. Nyborg, Effect of atomization on surface oxide composition in 316L stainless steel powders for additive manufacturing, *Surface and Interface, Analysis* 52 (2020) 694–706, <https://doi.org/10.1002/sia.6846>.
- [51] G. Salomonsen, N. Norman, O. L  nsj  , T.G. Finstad, Kinetics and mechanism of oxide formation on titanium, vanadium and chromium thin films, *J. Less Common Metals*. 158 (1990) 251–265, [https://doi.org/10.1016/0022-5088\(90\)90060-W](https://doi.org/10.1016/0022-5088(90)90060-W).
- [52] R.L. Higginson, C.P. Jackson, E.L. Murrell, P.A.Z. Exworthy, R.J. Mortimer, D.R. Worrall, G.D. Wilcox, Effect of thermally grown oxides on colour development of stainless steel, *Mater. High Temp.* 32 (2015) 113–117, <https://doi.org/10.1179/0960340914Z.00000000083>.
- [53] A.T. Sutton, C.S. Kriewall, M.C. Leu, J.W. Newkirk, B. Brown, Characterization of laser spatter and condensate generated during the selective laser melting of 304L stainless steel powder, *Addit. Manuf.* 31 (2020), <https://doi.org/10.1016/j.addma.2019.100904> 100904.
- [54] S. Vock, B. Kl  den, A. Kirchner, T. Wei  g  rber, B. Kieback, Powders for powder bed fusion: a review, *Prog. Addit. Manuf.* 4 (2019) 383–397, <https://doi.org/10.1007/s40964-019-00078-6>.
- [55] R. Williams, M. Bilton, N. Harrison, P. Fox, The impact of oxidised powder particles on the microstructure and mechanical properties of Ti-6Al-4 V processed by laser powder bed fusion, *Addit. Manuf.* 46 (2021), <https://doi.org/10.1016/j.addma.2021.102181> 102181.